Scilight

Photochemistry and Spectroscopy
https://www.sciltp.com/journals/ps

Article

Conformational Landscape, Infrared Characterization, and UV-Induced Reactivity of 3-Chloromethyl-5-(3-Methoxyphenyl)-1,2,4-Oxadiazole Isolated in a Nitrogen Matrix

İsa Sıdır [1,2], António J. L. Jesus [3,*] and Rui Fausto [2,4]

[1] Department of Physics, Faculty of Sciences and Letters, Bitlis Eren University, Bitlis 13000, Türkiye
[2] Department of Chemistry, CQC-IMS, University of Coimbra, 3004-535 Coimbra, Portugal
[3] Faculty of Pharmacy, CQC-IMS, University of Coimbra, 3000-548 Coimbra, Portugal
[4] Faculty of Sciences and Letters, Department of Physics, Istanbul Kultur University, Ataköy Campus, Bakırköy 34156, Türkiye
* Correspondence: ajorge@ff.uc.pt

How To Cite: Sıdır, İ.; Jesus, A.J.L.; Fausto, R. Conformational Landscape, Infrared Characterization, and UV-Induced Reactivity of 3-Chloromethyl-5-(3-Methoxyphenyl)-1,2,4-Oxadiazole Isolated in a Nitrogen Matrix. *Photochemistry and Spectroscopy* **2026**, *2*(3), 1. https://doi.org/10.53941/ps.2026.100022

Received: 27 December 2025
Revised: 1 February 2026
Accepted: 3 February 2026
Published: 3 July 2026

Abstract: In this study, we present a comprehensive analysis of the conformational landscape, vibrational properties and photochemistry of monomeric 3-chloromethyl -5-(3-methoxyphenyl)-1,2,4-oxadiazole (CMPO). This molecule can adopt eight different conformers, but only four of these (the *skew* conformers, with the chlorine atom tilted out of the oxadiazole ring plane) have significant populations in the gas phase. Comparison of the infrared spectrum of monomers of CMPO isolated in solid N_2 at 15 K with B3LYP/6-311++G(d,p) vibrational calculations, supports the presence of the four *skew* conformers in the as-deposited low-temperature N_2 matrix. UV measurements in various solvents reveal an intense absorption near λ = 255 nm, which TD-DFT calculations assign primarily to a $S_0 \rightarrow S_2$ $\pi \rightarrow \pi^*$ transition. UV irradiations of the matrix-isolated compound, using both narrowband ($\lambda = 255$ nm) and broadband ($\lambda > 220$ nm) light, induce N–O bond cleavage and ring opening, yielding carbodiimide (the favored species) and cyanamide as the isomerization photoproducts. No spectroscopic evidence of diazirine, nitrilimine, or 1,3,4-oxadiazole intermediates was detected. Photodecomposition also occurs, leading to the formation of isocyanate and 2-chloroacetonitrile. All the photoproduced species were identified by comparing the emerging IR bands with the computed vibrational spectra of the putative photoproducts.

Keywords: 1,2,4-Oxadiazoles; matrix isolation; IR spectroscopy; conformers, photochemistry

1. Introduction

Widely recognized as multifunctional heteroaromatic scaffolds, 1,2,4-oxadiazoles (top structure in Scheme 1) are valued for their structural adaptability and distinctive electronic properties [1]. These characteristics enable them to be extremely versatile in a variety of scientific fields [1–3]. In medicinal chemistry, 1,2,4-oxadiazoles often serve as bioisosteric substitutes for amide, ester, and carbamate groups, improving metabolic stability, modulating lipophilicity, and enhancing target affinity [4,5]. As a result, numerous derivatives display broad-ranging biological activities [1,3,6–8], including antimicrobial [3,4], anticancer [5,6], anti-inflammatory [7] and neuroprotective [8,9] effects, establishing this heterocycle as an attractive platform in drug discovery.

In addition to their medicinal applications, 1,2,4-oxadiazoles are also important in agrochemistry, where they constitute key scaffolds in modern herbicides and insecticides [9]. They are also widely used in materials science as, for example, building blocks for liquid crystals and organic semiconductors, sensors, energetic materials, as well as for optoelectronic devices, such as organic light emitting diodes (OLEDs) [1,3,10]. Moreover, these compounds can serve as versatile ligands in coordination chemistry, enabling the formation of metal complexes relevant to catalysis and photophysical studies [11].

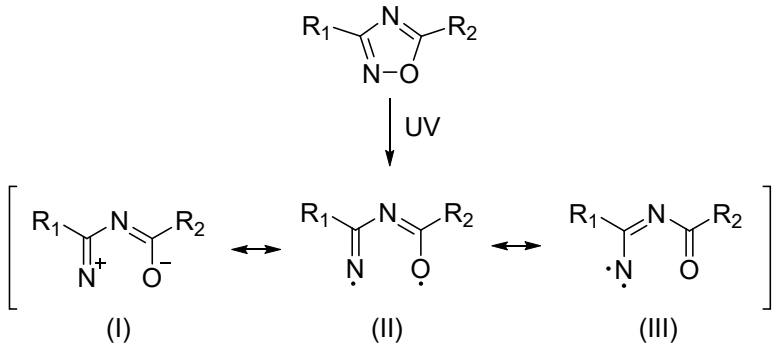

Scheme 1. Proposed primary photolytic intermediate formed upon N−O bond cleavage in 1,2,4-oxadiazole-containing compounds, as established in Ref. [12].

The unique electronic structure of the 1,2,4-oxadiazole ring also makes these compounds particularly interesting from a photochemical standpoint. The experimental studies reported so far have been carried out mostly in solution under UV-irradiation [12–20] and complemented by computational studies aimed at elucidating the underlying mechanisms [21–23]. In addition, a few reviews covering the photochemistry of 1,2,4-oxadiazoles have also been published [1,3,24]. Typically, the first photochemical event following UV-excitation involves cleavage of the labile N–O bond, producing a highly reactive open-chain intermediate that may adopt zwitterionic (I), diradical (II), or nitrene-like (III) character [12], see Scheme 1. Depending on the substitution pattern, reaction medium, and the presence of other species, this intermediate can evolve into diverse products. Among the documented outcomes are 1,3,4-oxadiazoles, formed from 3-amino-substituted derivatives under basic conditions [19]; isomeric 1,2,4-oxadiazoles with rearranged substitution patterns [14]; and quinazolinone systems, generated from 5-aryl substituted derivatives [13].

Despite these advances, solvent-free photochemical behaviour of these compounds remains largely unexplored. To the best of our knowledge, only one study has addressed this aspect: the photolysis of 1,2,4-oxadiazole-3,5-diamine (R_1, R_2 = NH_2) in low-temperature argon and krypton matrices [25]. Irradiation of the matrix-isolated compound at 213 and 220 nm led to its photodecomposition into aminoformonitrile oxide (H_2NCNO) and aminoisocyanate (H_2NNCO), both complexed with cyanamide (H_2NCN). In addition, the study reported the spectroscopic detection of diazenecarbaldehyde (HNNCHO). This species, also observed as a complex with H_2NCN, was shown not to originate from photoisomerization of H_2NNCO but rather to form through an independent reaction pathway.

Building on our recent photochemical studies on matrix-isolated 1,3,4-oxadiazoles, such as pyridyl-substituted 1,3,4-oxadiazole-thione [26] and 2-amino-5-(4-methoxyphenyl)-1,3,4-oxadiazole [27], we now broaden our research to the 1,2,4-oxadiazole scaffold. Specifically, we investigate 3-chloromethyl-5-(3-methoxyphenyl)-1,2,4-oxadiazole (CMPO). To date, no data are available on its conformational preferences, vibrational characteristics, or intrinsic photochemistry. To address these gaps, we performed a matrix-isolation study of CMPO in solid nitrogen at 15 K. Infrared spectroscopy combined with DFT calculations enabled detailed conformational analysis and vibrational assignments. Subsequent narrowband and broadband UV irradiations revealed that CMPO photochemistry is dominated by isomerization to carbodiimide and cyanamide, accompanied by photodecomposition yielding isocyanate and 2-chloroacetonitrile.

2. Methods

2.1. Experimental Methods

Commercial 3-chloromethyl-5-(3-methoxyphenyl)-1,2,4-oxadiazole (CMPO, **1**) was purchased from Sigma-Aldrich with a stated purity greater than 99% and used without further purification (m.p. = 58–59 °C). High purity N_2 (99.99%) was employed as host gas. A small quantity of the solid compound was placed inside a miniature glass oven which was then attached to the vacuum chamber of a closed-cycle helium cryostat (APD Cryogenics,

with a DE-202 A expander). Before cooling the cryostat, the sample was pumped to remove volatile impurities. The pressure inside the vacuum chamber goes down to ~5.7×10^{-5} mbar. To prepare a low-temperature matrix, the compound was sublimated slightly above the room temperature using thermoelectric heating provided by a Vitecom DC Power Supply 75-HY5003 model. The highest current and potential applied during the deposition were approximately 0.23 A and 1.2 V. The resulting vapors were then co-deposited with a large excess of N_2 onto a CsI optical substrate, cooled down to 15 K. The temperature of the CsI window was measured directly at the sample holder by using a silicon diode sensor connected to a digital controller (Scientific Instruments, model 9650-1, West Palm Beach, FL, USA), ensuring temperature stabilization with an accuracy of ±0.1 K.

IR spectra of the matrix-isolated compound were recorded using a Thermo Nicolet 6700 FTIR spectrometer, equipped with a deuterated triglycine sulphate (DTGS) detector and a Ge/KBr beam splitter. To prevent interference from atmospheric H_2O and CO_2, the spectrometer was continuously purged with a stream of dry, CO_2-filtered air.

UV irradiation experiments, using both narrowband and broadband sources, were performed through the outer quartz window of the cryostat. Narrowband (fwhm = 0.2 cm^{-1}) irradiations (λ = 255 nm; different exposure times) were undertaken using the frequency-doubled signal beam of a Quanta-Ray MOPO-SL optical parametric oscillator (OPO), pumped with a pulsed Nd:YAG laser PRO 230 from Spectra-Physics (repetition rate = 10 Hz, pulse energy ~1–3 mJ, duration = 10 ns). Broadband irradiations were carried out using a 500 W Hg(Xe) arc lamp (Newport, Oriel Instruments) with the output power set to 200 W, filtered through water (λ > 220 nm).

UV spectra of CMPO in solution were recorded in the 190–400 nm wavelength range using a Perkin Elmer Lambda-35 UV-Vis spectrophotometer. All measurements were performed using a quartz cell (standard cell, with 1 cm × 1 cm optical path), at room temperature. The solvents employed: cyclohexane, acetonitrile, and methanol, were of spectroscopic grade and purchased from Sigma-Aldrich.

2.2. Computational Methods

Quantum mechanical computations were carried out using Gaussian 16 (Revision B.01) [28] suite of programs. The geometries of the reactants and photoproducts were fully optimized using the DFT(B3LYP) [29–31] hybrid functional in combination with the 6-311++G(d,p) basis set [32,33], followed by harmonic vibrational frequency calculations at the same level of theory. All geometries were optimized under "tight" convergence criteria. Each optimized structure was verified as a true minimum through Hessian matrix analysis, confirming that no imaginary (negative) vibrational frequencies were present. For interpretation of the experimental results, the wavenumber and IR intensities extracted from the B3LYP/6-311++G(d,p) vibrational calculations were used. To account for basis set limitations, vibrational anharmonicity, and neglected part of the electron correlation, the calculated wavenumbers were multiplied by 0.960 or 0.980 for the vibrational modes above or below 2000 cm^{-1}, respectively. For graphical comparison with the experimental spectra, the calculated wavenumbers (scaled) and IR intensities (in km mol^{-1}) were convoluted using Lorentzian functions with a full-width-at-half-maximum (FWHM) of 4 cm^{-1}. The vibrational analysis was helped by using the vibrations' animation module of Chemcraft (version 1.8) [34] or GaussView 6.0.16 [35]. Theoretical UV absorption spectra of the most relevant conformers of CMPO (**1**) were obtained from TD-DFT [36] calculations at the B3LYP/6-311++G(d,p) level, where each electronic transition was convoluted with a Lorentzian function (full width at half maximum, FWHM = 0.33 eV).

3. Results and Discussion

3.1. Conformational Landscape and Interconversion Energy Barriers for the Title Molecule

The CMPO (**1**) molecule exhibits eight distinct conformers (Figure 1), each labeled by a three-letter code that reflects, in order, the conformations of the C13−O12−C8−C7, C7−C6−C5−O1, and Cl15−C14−C3−N2 dihedral angles. *Anti* (~180°), *syn* (~0°), and *skew* (~120°) conformations are abbreviated as **A**, **S**, and **Sk**. The first dihedral characterizes the orientation of the methoxy group relative to the molecular scaffold which can be either *syn* or *anti*. The second dihedral specifies the relative arrangement of the two C−O bonds (in the methoxy and 1,2,4-oxadiazole fragments), resulting from rotation about the inter-ring C5−C6 single bond, and likewise alternates between *syn* and *anti*. The third dihedral characterizes the orientation of the C−Cl bond with respect to the in-plane C3−N2 bond, giving rise to two possible stable conformations, namely *skew* and *syn* (Figure 2).

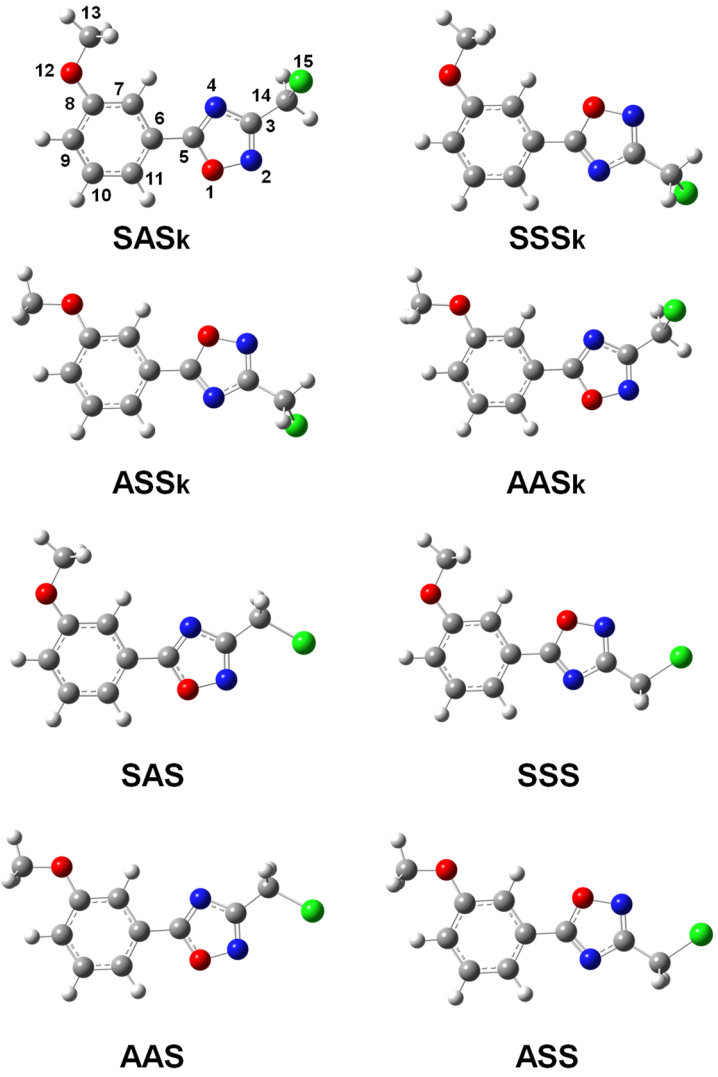

Figure 1. Geometries of the eight conformers of CMPO (**1**) fully optimized at the B3LYP/6-311++G(d,p) level of theory. Atom numbering scheme is given in the most stable conformer **SASk**.

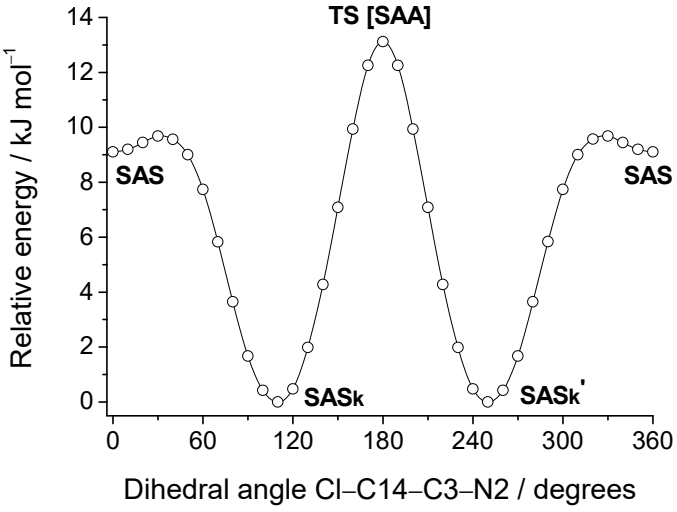

Figure 2. B3LYP/6-311++G(d,p) relaxed potential energy surface for rotation of the chloromethyl group about the C14−C3 bond, with the C13−O12−C8−C7 and C7−C6−C5−O1 dihedrals maintained in ***syn*** and ***anti*** orientations, respectively. **SASk** and **SASk′** are mirror-image conformers, interconnected through the first-order transition state **TS[SAA]**.

The geometries of the eight conformers were fully optimized at the B3LYP/6-311++G(d,p) level and the electronic (ΔE_{el}), zero-point corrected (ΔE_0), and standard Gibbs free energies (ΔG^0) extracted from these calculations are summarized in Table 1, together with the Boltzmann populations (298.15 K) and dipole moments of the optimized structures. The computational data reveal a clear energetic separation between two families of conformers differing from each other by the orientation of the chloromethyl group. The *skew* family (**SASk**, **SSSk**, **ASSk**, and **AASk**, all with C_1 symmetry) is markedly more stable, while the planar family (**SAS**, **SSS**, **AAS**, and **ASS**, all with C_s symmetry) lies 6.2, 5.7 or 4.7 kJ mol^{-1} higher in energy, depending on whether electronic, zero-point, or standard Gibbs energies are considered. In the skew family, the chlorine atom is tilted out of the oxadiazole ring plane (Cl−C14–C3–N2 ≈ 108–109°), resulting in a more favorable arrangement that reduces the electrostatic repulsion of Cl with the ring nitrogen atoms. Within this family, the relative stability of the conformers is mainly dictated by the orientation of the methoxy group, with the *syn* configuration being favored over the *anti* by ~2 kJ mol^{-1}, while rotation around the central C5−C6 bond exerts only a minor energetic effect. The global minimum corresponds to conformer **SASk**, followed closely by **SSSk** (ΔG^0 = 0.55 kJ mol^{-1}); together, these two forms account for 65% of the gas-phase equilibrium conformational mixture at 298.15 K, while **AASk** and **ASSk**, which have nearly identical gas-phase populations, both contribute an additional ~31%.

Table 1. Relative electronic energies (ΔE_{el}), zero-point corrected energies (ΔE_0), standard Gibbs energies (ΔG^0), Boltzmann populations and dipole moments (μ) of the conformers of **1** computed at the B3LYP/6-311++G(d,p) level of theory. [a]

Conf.	Sym.	ΔE_{el}	ΔE_0	ΔG^0	Pop. (%)	μ (Debye)
SASk	C_1	0.00	0.00	0.00	36.29	2.97
SSSk	C_1	0.82	0.64	0.55	29.12	3.02
ASSk	C_1	2.64	2.30	2.07	15.72	4.79
AASk	C_1	2.89	2.47	2.12	15.42	4.80
SAS	C_s	9.11	8.19	6.85	1.14	4.35
SSS	C_s	9.14	8.12	6.89	1.13	3.28
AAS	C_s	11.26	9.96	8.46	0.60	5.76
ASS	C_s	11.29	10.03	8.51	0.59	5.78

[a] All Energies in kJ mol^{-1}. The standard Gibbs energies and Boltzmann populations (estimated from the Gibbs energies) are reported at 298.15 K. See Figure 1 for schematic representation of the conformers.

The four less stable conformers, in which the C–Cl bond adopts a *syn*-periplanar orientation relative to the C3–N2 bond, account for only ~4% of the overall gas-phase equilibrium population, and their relative energetic ordering parallels that observed for the *skew* family. It is noteworthy that conformations where the C–Cl bond is *anti*-periplanar to the C3−N2 bond do not correspond to minima but to transition-state structures on the potential energy surface interconnecting the two-symmetry related *skew* conformers (see Figure 2). This behavior can be readily understood by considering that the strongly electronegative oxygen atom (O1) withdraws electron density from the adjacent N2 atom, resulting in a partial charge at this atom (−0.143 to −0.146, obtained from Natural Population Analysis) that is significantly less negative than that at N4 (−0.507 to −0.529), which retains a more localized lone pair. Consequently, when the C–Cl bond points toward N2, the chlorine atom (δ^-) faces a less negative electrostatic environment, thereby stabilizing the conformation. Conversely, when the C–Cl bond is directed toward N4, the chlorine atom approaches a highly electron-dense region, where lone-pair/lone-pair repulsion between Cl and N4 destabilizes the system, giving rise to a transition-state (TS) geometry.

From the above discussion, only the *skew* conformers of **1** possess sufficiently high gas-phase populations to be efficiently trapped in the low-temperature N_2 matrix. However, to determine whether all four conformers can indeed be preserved under cryogenic conditions, it is also necessary to evaluate the energy barriers governing their interconversion, which were calculated from the B3LYP/6-311++G(d,p) potential energy profiles corresponding to internal rotations about the C8–O12 and C5–C6 bonds. The calculated scans, shown in Figure 3, reveal barrier heights for the relaxation pathways from higher- to lower-energy conformers of approximately 13 kJ mol^{-1} for rotation around the C8–O12 bond and 25–27 kJ mol^{-1} for rotation about the C5–C6 bond. These barriers are sufficiently large to preclude any over-the-barrier conformational interconversion during deposition of the matrices under the experimental conditions employed in the performed matrix isolation experiments (15 K). Consequently, all four *skew* conformers can be expected to be effectively trapped in the deposited N_2 matrix.

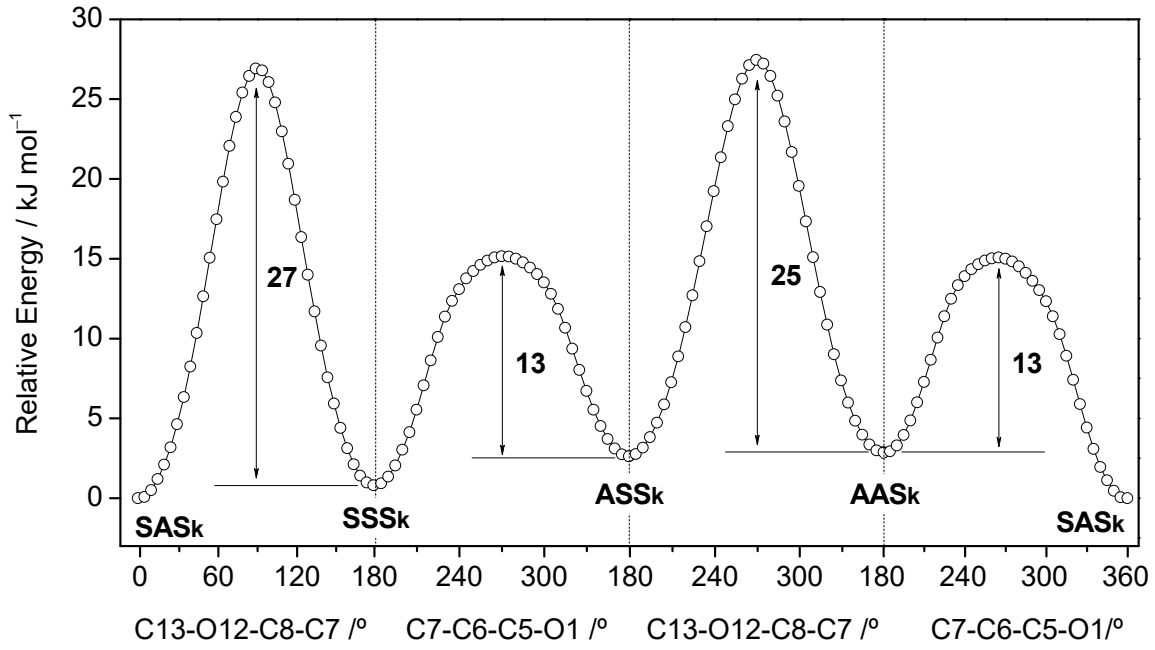

Figure 3. B3LYP/6-311++G(d,p) energy profiles for the interconversion among the four most stable conformers of **1**, arising from internal rotations about the C13−O12−C8−C7 or C7−C6−C5−O1 dihedral angles. The electronic energy profiles were obtained from relaxed potential energy surface (PES) scans, in which the dihedral angle was incrementally varied while all other internal coordinates were optimized at each step. For each pair of conformers, the interconversion barrier is shown as the energy difference between the transition state and the higher energy conformer.

3.2. Infrared Spectrum of CMPO Isolated in Solid N_2 at 15 K

Molecules of CMPO (**1**) were isolated in a cryogenic N_2 matrix at 15 K by direct deposition of vapors generated through sublimation of the compound, as described in the Experimental Section. Figure 4a presents the infrared spectrum recorded after the matrix deposition, which is compared with the theoretical gas-phase spectrum of the compound shown in Figure 4b. The latter was simulated using vibrational data computed for the four most stable conformers **SASk**, **SSSk**, **ASSk**, and **AASk**. Individual stick spectra for these conformers are provided in Figure 4c,d. In constructing the composite theoretical gas-phase spectrum, the calculated IR intensities of the individual conformers were scaled by factors of 1, 0.8, 0.4, and 0.4, respectively, according to their gas-phase populations (see Table 1), to reflect their expected relative abundances under matrix-isolation conditions. The resulting simulated profile reproduces both the band positions and relative intensities observed experimentally, confirming that the as-deposited matrix contains a mixture of the four skew conformers in proportions reasonably consistent with the theoretical predictions. The presence of all four conformers in the as-deposited matrix is also consistent with the magnitude of the energy barriers separating them, which prevents conformational relaxation during the matrix deposition at 15 K [37–41]. A tentative vibrational assignment of the experimental spectrum was carried out, and the results are summarized in Table 2. These assignments were supported by detailed comparison between the experimental N_2-matrix spectrum (15 K) and the vibrational data computed for the conformers.

Due to the extensive overlap among the vibrational modes predicted for the four trapped conformers, a confident attribution of a given experimental band to a specific conformer, or subset of conformers, is not straightforward. Therefore, only a tentative attribution can be made based on spectral comparison, as provided in Table 2. In an attempt to induce conformational changes in the matrix-isolated molecule, which could enable a more reliable identification of the conformers, we annealed the N_2 matrix up to its thermal stability limit (~30 K). However, no spectral changes were observed that could be attributed to conformational relaxations. This behavior is not surprising considering our previous study on 2-amino-5-(4-methoxyphenyl)-1,3,4-oxadiazole [27], where annealing the compound isolated in a Xe matrix up to 65 K did not alter the populations of the conformers. In that case, the conformers were separated by energy barriers of approximately 23 and 14 kJ mol^{-1}, corresponding, respectively, to inter-ring C–C rotamerization and methoxy group rotation, values close to those computed for the present molecule (see Figure 3).

Table 2. Experimental IR spectra (N_2 matrix, 15 K) compared with the B3LYP/6-311++G(d,p) vibrational frequencies (ν, cm^{-1}) and infrared intensities (I^{IR}, km mol^{-1}) calculated for the conformers of **1** expected to be present in the deposited matrix and approximate vibrational assignments. [a]

N_2, 15 K	Calc. SASk		Calc. SSSk		Calc. ASSk		Calc. AASk		Approximate Assignment
ν_{Exp}	$\nu_{Calc.}$	I^{IR}	$\nu_{Calc.}$	I^{IR}	$\nu_{Calc.}$	I^{IR}	$\nu_{Calc.}$	I^{IR}	
1614			1610	39.5	1619	10.9	1616	25.0	νCC ph
1605	1605	60.9							νCC ph
	1604	56.5							νCC ph
1594			1596	5.9	1590	16.6	1595	107.3	νCC ph
1573/1568	1563	145.2	1569	262.3	1567	299.6	1566	131.9	νC5 = N4
1524	1519	8.9	1518	16.2	1519	15.6	1518	7.2	νC3 = N2
1495/1491			1491	78.9	1487	76.3			δCH ph
1485	1481	55.6							δCH ph; νCC ph
1472	1473	93.4	1474	54.7	1474	37.9	1475	27.8	δCH_3 as
							1476	82.3	δCH ph; νCC ph
1460	1464	10.3	1464	10.3	1464	9.8	1464	9.7	δCH_3 as'
	1457	4.1	1450	6.4	1447	3.1	1455	51.7	δCH_3 s
1437	1440	39.9	1441	38.5	1441	35.9	1440	34.7	δCH_2
	1433	60.4					1439	62.2	δCH_3 s
1422			1421	17.2	1430	15.9			δCH ph; νCC ph
1383/1378	1376	158.7	1378	179.1	1377	165.8	1376	158.7	νC3=N4
1331	1337	57.1	1337	44.9					δCH ph; νCC ph
1324					1332	39.1	1331	10.1	δCH ph; νCC ph
1302	1292	21.2	1309	5.9	1303	1.8	1296	120.5	δCH ph
1295/1293	1282	110.3	1279	22.0	1287	124.1			νC5−O1; δCH ph; νCC ph
1273	1276	33.4	1276	78.3	1276	43.3	1277	35.2	wCH_2
							1272	40.8	νC5−O1; δCH ph; νCC ph
1245	1236	83.0					1234	108.8	νC8−O12 + νC5−O1
1238			1229	188.8					νC8−O12 + νC5−O1
1223					1218	152.2			νC8−O12 + νC5−O1
1187	1179	5.5	1180	11.4	1178	10.9	1177	4.8	ρCH_3
1164	1164	5.7	1161	13.1	1171	2.0	1173	1.4	δCH ph
	1161	12.7	1161	4.0	1161	15.3	1161	16.2	$twCH_2$
1112	1109	23.2	1109	1.9					νC5−O1; δCH ph
1106					1104	9.6			νC5−O1; δCH ph
1101							1099	35.2	νC5−O1; δCH ph
							1095	10.9	δCH ph
1084	1084	10.4							δCH ph; νCC ph
					1081	38.0			νCC ph; δCH ph; νC5−O1
1076			1073	21.5					δCH ph; νCC ph
1055					1053	85.4	1049	100.7	νC13−O12
1048	1040	57.8	1041	46.0					νC13−O12
1018	1021	4.5	1018	5.7	1017	1.9	1019	2.0	νC3−N4
996	990	6.0	992	11.9	989	0.7	989	2.6	δ ph
991/987/983	983	1.5	988	0.5	986	3.9	982	3.2	δ ox
925	923	5.9	922	7.5	923	6.1	923	4.2	νN−O
904/898	901	0.1	906	0.0	893	10.3	898	10.9	γCH ph
	897	2.3	896	2.5	897	2.0	896	5.7	ρCH_2
884					880	6.6	878	1.8	γC ph; γCH ph
874	874	17.0							γC ph; γCH ph
865/861			862	19.1					γC ph; γCH ph
			857	55.7					δ ph
856	851	48.1							δ ph
848					844	35.1			δ ph
845							837	25.2	δ ph
804	797	12.3	799	15.1					γC ph; γCH ph; γC ox
796					794	6.5	790	4.3	γC ph; γCH ph; γC ox
779	780	22.1	778	20.8	773	28.6	774	33.5	γC ox; γC ph; γCH ph
756	736	51.1	732	50.0	734	38.5	736	60.0	νC3−C14
738	726	50.7	725	38.1	728	54.5	726	48.7	γC ox; νC−Cl
	681	10.8	678	12.4	677	7.1	676	1.9	γC ph; γCH ph
685/679/676	672	8.1	672	8.0					δ ph
					674	17.2	673	15.3	γC ph
643	632	12.0	632	13.6	632	14.2	632	13.0	γC ox; γN ox
567	564	5.0	563	4.2	565	8.2	564	5.7	δCOC

[a] Calculated harmonic wavenumbers (in cm^{-1}) were multiplied by 0.980. Abbreviations: ν = stretching, δ = in-plane bending, γ = out-of-plane deformation, w = wagging, ρ = rocking, tw = twisting, s = symmetric, as = antisymmetric; ph = phenyl ring; ox = 1,2,4-oxadiazole ring. Sign "+" designates combination of vibrations occurring in the same phase.

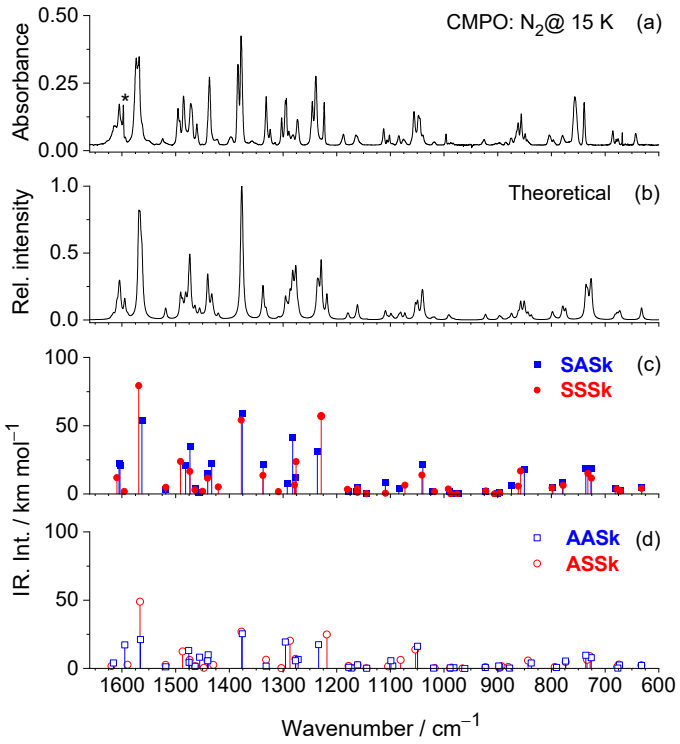

Figure 4. (**a**) Experimental IR spectrum of CMPO (**1**) isolated in an N_2 matrix at 15 K. The band marked with an asterisk is due to matrix isolated water impurity. (**b**) Theoretical gas-phase IR spectrum of **1**, simulated from the B3LYP/6-311++G(d,p) vibrational data computed for the four most stable conformers as detailed in the text. (**c**,**d**) Scaled wavenumbers and IR intensities calculated for the four most stable conformers of **1**.

*3.3. UV-induced Transformations of **1***

The UV spectra of **1** in different solvents, exhibiting distinct characteristics (non-polar: cyclohexane; polar-aprotic: acetonitrile; polar-protic: methanol) were recorded and are shown in Figure 5. In this figure, the experimental spectra are compared with the theoretical absorption spectra of the four skew conformers of the molecule, which were simulated from TD-DFT/B3LYP/6-311+G(d,p) calculations. As shown, the theoretical UV spectra are very similar for all four *skew* conformers and reproduce well the experimental spectra obtained in the different solvents. The calculated data (excitation wavelengths, oscillator strengths and main contributors to the transitions) for the different conformers are summarized in Table 3, and the main orbitals involved represented in Figure 6.

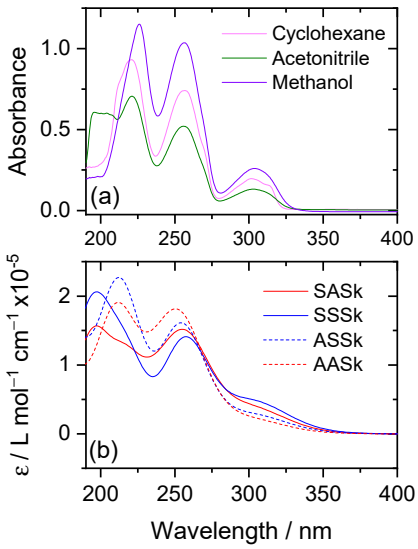

Figure 5. (**a**) Experimental UV spectra of CMPO (**1**) in different solvents (feature at about 200 nm in acetonitrile is due to solvent). (**b**) TD-DFT/B3LYP/6-311++G(d,p) predicted gas-phase UV-vis spectra of the four skew conformers of **1**.

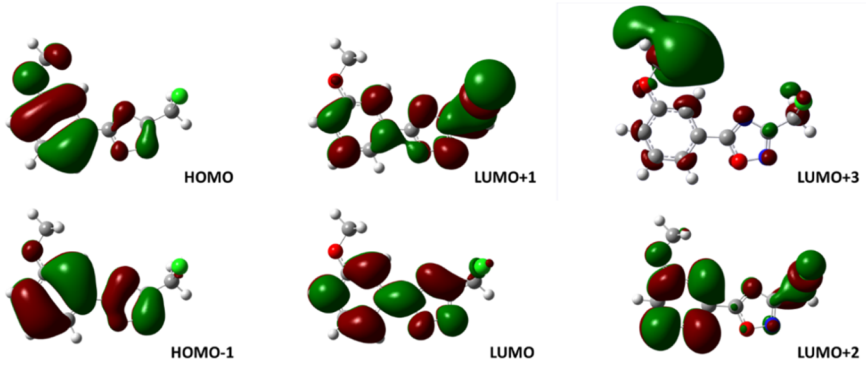

Figure 6. DFT/B3LYP/6-311++G(d,p) calculated molecular orbitals involved in the relevant excitations observed in the UV-vis spectra of **1**. The orbitals correspond to the most stable conformer **SASk**; similar results were obtained for the remaining *skew* conformers of the molecule; see Table 3. Isovalue for the surfaces: 0.02.

Table 3. TD-DFT/B3LYP/6-311++G(d,p) predicted gas-phase UV-vis wavelengths (λ), oscillator strengths (f) and description of the 13 lowest energy singlet excitations for the skew conformers of **1**.[a]

	SASk			**AASk**		
State	λ	f	**Description** [b]	λ	f	**Description** [b]
S_1	303.6	0.0859	H → L (67%)	302.3	0.0485	H → L (68%)
S_2	259.7	0.3058	H-1 → L (63%)/H → L + 2 (16%)	256.4	0.3466	H-1 → L (65%)/H → L + 2 (12%)
S_3	239.6	0.1436	H → L + 1 (65%)/H-1 → L (22%)	237.9	0.1828	H → L + 1 (65%)/H-1 → L (22%)
S_4	231.9	0.0026	H-4 → L (64%)	232.6	0.0026	H-4 → L (65%)
S_5	219.7	0.0331	H-2 → L (46%)/H-1 → L + 1 (35%)	222.8	0.0044	H → L + 3 (70%)
S_6	218.1	0.0154	H → L + 3(64%)/H-3 → L (17%)	220.5	0.0197	H-2 → L (41%)/H → L + 2 (17%)
S_7	217.8	0.0640	H-3 → L (49%)	218.0	0.0037	H-2 → L (44%)/H-3 → L (42%)
S_8	216.8	0.1176	H-2 → L (40%)/H-5 → L (10%)	216.2	0.2205	H → L + 2 (56%)/H-3 → L (25%)
S_9	213.7	0.0174	H-1 → L + 1 (45%)	214.3	0.0775	H-1 → L + 1 (40%)/H → L + 2 (24%)
S_{10}	206.0	0.0061	H → L + 5 (50%)	204.4	0.0145	H → L + 5 (58%)
S_{11}	202.4	0.0122	H → L + 4 (60%)/H → L + 5 (33%)	203.0	0.1906	H-1 → L + 2 (58%)
S_{12}	200.3	0.0612	H-5 → L (46%)/H-1 → L + 1 (27%)	201.7	0.0108	H → L + 4(44%)/H → L + 5 (34%)
S_{13}	197.1	0.2069	H-1 → L + 2 (58%)	199.5	0.0189	H-5 → L (58%)/H-1 → L + 1 (25%)
	SSSk			**ASSk**		
State	λ	f	**Description** [b]	λ	f	**Description** [b]
S_1	304.5	0.1090	H → L (67%)	303.8	0.0643	H → L (68%)
S_2	257.7	0.3395	H-1 → L (65%)/H → L + 2 (20%)	255.1	0.3868	H-1 → L (68%)/H → L + 2 (17%)
S_3	238.0	0.0025	H → L + 1 (68%)/H → L + 2 (14%)	235.1	0.0009	H → L + 1(66%)/H → L + 2 (20%)
S_4	233.2	0.0025	H-4 → L (64%)	232.8	0.0026	H-4 → L (64%)
S_5	221.8	0.1519	H → L + 1 (49%)/H-2 → L (21%)	223.2	0.0051	H → L + 3 (70%)
S_6	219.7	0.0057	H → L + 3 (64%)/H-2 → L (23%)	221.5	0.1988	H → L + 2 (49%)
S_7	219.6	0.0150	H-2 → L (59%)/H-4 → L (12%)	219.0	0.0555	H-2 → L (53%)/H-3 → L (30%)
S_8	218.2	0.0023	H-3 → L (57%)/H-2 → L (23%)	217.8	0.0017	H-3 → L (56%)/H-1 → L + 1 (21%)
S_9	212.2	0.1379	H-1 → L + 1 (49%)	212.2	0.2154	H-1 → L + 1 (50%)/H → L + 2 (15%)
S_{10}	206.3	0.0067	H → L+5(49%)	205.0	0.0550	H → L + 4 (51%)/H → L +5(28%)
S_{11}	203.0	0.0415	H → L + 4 (50%)/H → L + 5 (42%)	204.1	0.1070	H-1 → L + 2 (40%)
S_{12}	200.1	0.1735	H-5 → L (41%)/H-1 → L + 1 (30%)	201.8	0.0029	H → L + 5 (48%)/H → L + 6 (39%)
S_{13}	196.9	0.0037	H-2 → L + 1 (66%)	198.2	0.0844	H-5 → L (43%)/H-1 → L + 2(35%)

[a] The alternating white and gray colors of the background group the transitions according to their contribution to the observed bands at wavelengths around 300 nm, 255 nm and two overlapped bands in the 200–220 nm region (see Figure 5). [b] H: HOMO; L: LUMO; only major contributors are shown.

The experimental spectra recorded in the various solvents are similar, exhibiting a lower intensity band at longer wavelengths (ca. 300 nm), which is assigned to the HOMO → LUMO transition ($S_0 \rightarrow S_1$, of $\pi\pi^*$ character), and three intense bands, one at ca. 255 nm and two overlapping bands within the 200–220 nm range. The 255 nm band is essentially due to the $S_0 \rightarrow S_2$ transition, with an additional contribution from the $S_0 \rightarrow S_3$ transition, which accounts for the shorter wavelength wing of this absorption band. Both $S_0 \rightarrow S_2$ and $S_0 \rightarrow S_3$ transitions are of $\pi\pi^*$ character and involve major contributions from the HOMO-1 → LUMO/HOMO → LUMO + 2 and HOMO → LUMO + 1/HOMO-1 → LUMO excitations, respectively (see Table 3). As shown in Figure 6, these excitations have some character of charge transfer from the ring system to the C-Cl bond. The overlapping bands at shorter wavelengths have contributions from transitions from the ground state to several higher order excited states (S_5 to S_{13}). The major contributions to these bands and the involved orbitals are identified in Table 3.

Based on the UV spectrum of the studied compound, narrowband irradiation at λ = 255 nm primarily promotes excitation to the S_2 state, whereas broadband irradiation accesses excited states up to S_6. The results obtained using the two irradiation sources were found to be essentially identical (Figure S1). Therefore, only the results from the UV-laser experiments are used in the following discussion.

Figures 7 and 8 present the difference spectra obtained by subtracting the spectrum of the as-deposited N_2 matrix from that recorded after 60 min of UV laser irradiation (λ = 255 nm), together with the B3LYP-simulated spectra of **1** (shown as negative features) and of the identified photoproducts (shown as positive features), in the 2300–2100 cm^{-1} and 1800–675 cm^{-1} regions, respectively. Scheme 2 summarizes the proposed photochemical reaction pathway of matrix-isolated **1**, as inferred from the spectroscopic observations and supported by the computational results. The calculated structures of the most stable conformers of each putative photoproduct are shown in Figure 9, while their relative energies, including those of the different conformers, are compiled in Table S1. The vibrational band assignments for the identified photoproducts are summarized in Table 4. Additional calculated structural and vibrational data for the photoproducts, whether experimentally observed or not, are provided in the Supporting Material (See Tables S2 and S3 and Computational data).

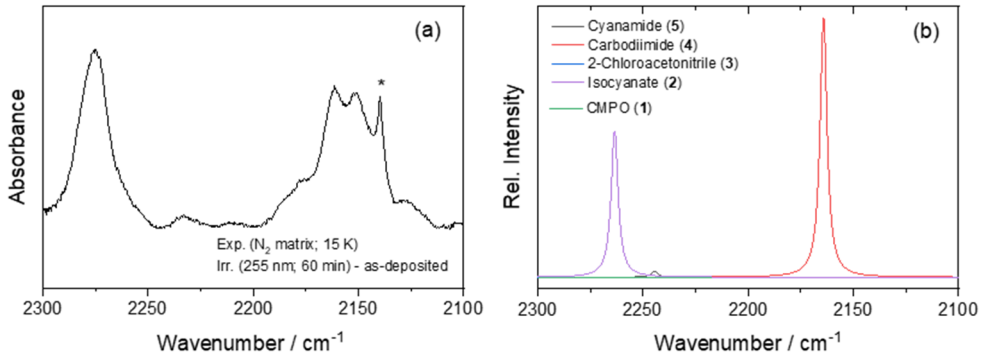

Figure 7. (**a**) Difference IR spectra in the 2300–2100 cm^{-1} obtained by subtracting the spectrum of the as-deposited matrix to that obtained after 60 min of narrowband UV-irradiation (λ = 255 nm), and (**b**) B3LYP-simulated spectra of the identified photoproducts. Reactant CMPO (**1**) does not absorb in this region and 2-Chloroacetonitrile (**3**) exhibits a very weak absorption at 2314 cm^{-1} ($\nu C{\equiv}N$, I^{IR} = 0.4 km mol^{-1}). Intensities of the photoproducts **5**:**4**:**2** in a ratio 1:2:1.5 (see text). Band marked with * is due to CO.

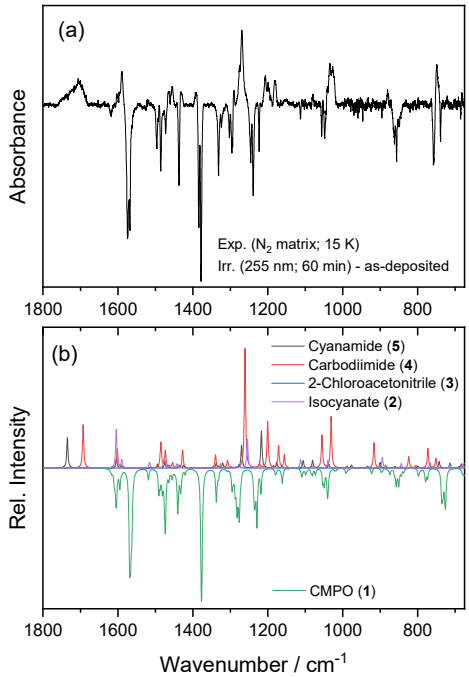

Figure 8. (**a**) Difference IR spectra in the 1800–675cm^{-1} region obtained by subtracting the spectrum of the as-deposited matrix from that obtained after 60 min of narrowband UV-irradiation (λ = 255 nm), and (**b**) B3LYP-simulated spectra of **1** (downward) and of the identified photoproducts (upward). Intensities of the photoproducts **5**:**4**:**3**:**2** in a ratio 1:2:1.5:1.5 (see text).

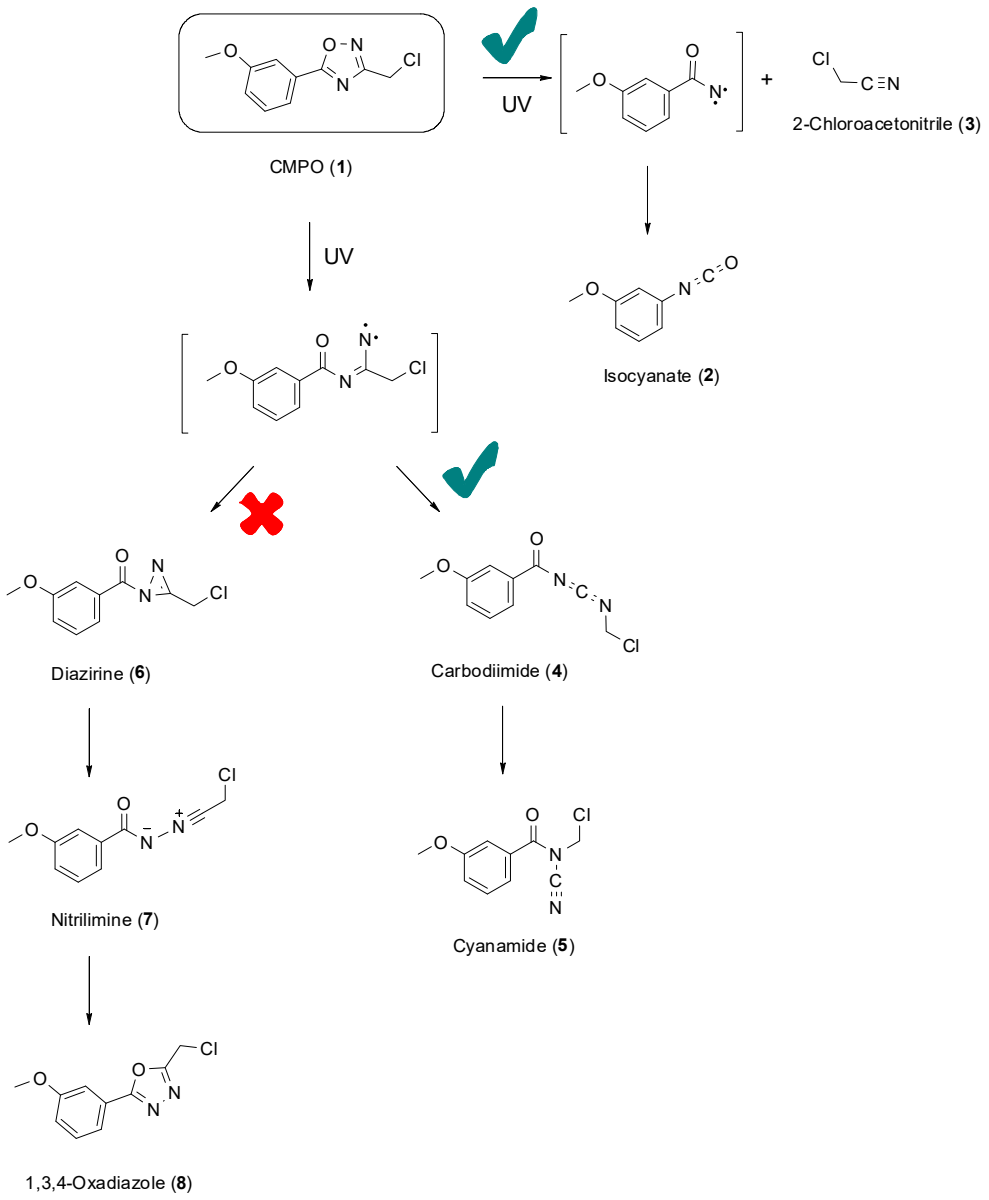

Scheme 2. Proposed mechanism for the photochemistry of CMPO (**1**) isolated in solid N_2. The acylnitrene and imidoylnitrene intermediates, as well as species **6**, **7** and **8**, were not observed.

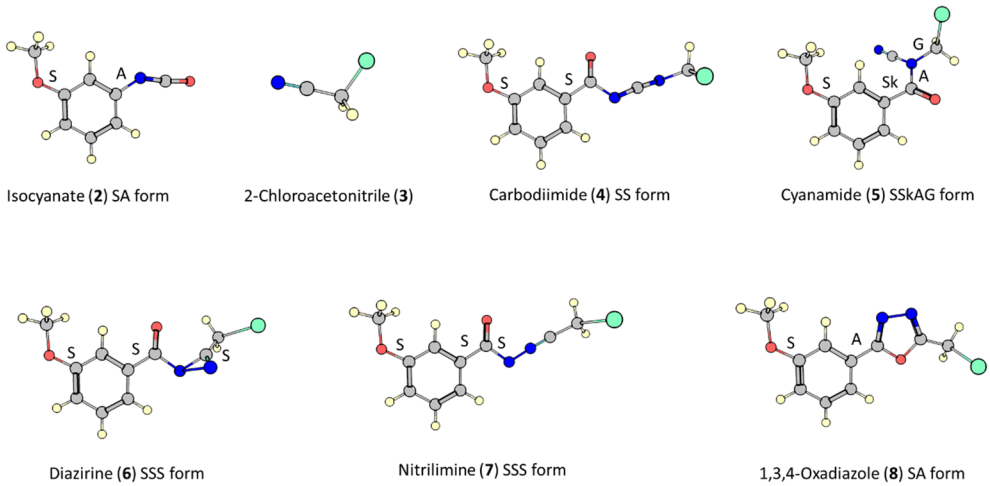

Figure 9. DFT/B3LYP/6-311++G(d,p) calculated optimized geometries for the most stable conformers of the putative photoproducts of **1**. The conformers are labelled according to the torsional arrangements about a selected bond, from left to right: A = *anti*; S = *syn*; G = *gauche*; Sk = *skew*. All other torsional angles remain unchanged across the conformers of a given photoproduct and, thus, are not explicitly specified.

Table 4. Assignments for the observed bands of the photoproducts of **1**. [a]

Exp.	Calculated, DFT/B3LYP/6-311++G(d,p)											
	Carbodiimide 4			Cyanamide 5			Isocyanate 2			2-Chloroacetonitrile 3		
ν	ν	I^{IR}		ν	I^{IR}		ν	I^{IR}		ν	I^{IR}	
2275							2263	1802	νO=C=N as			
2234				2244	114	νNCN as						
2183/2176 2161/2152 2128	2164	2399	νNCN as									
1728				1735	325	νC=O						
1704	1693	230	νC=O									
1602							1605	273	νC=C ring			
1595				1604	98	νC=C ring						
1590	1602	103	νC=C ring									
1519							1516	41	νO=C=N s			
1465	1485	132	νNCN s									
1447	1473	91	δCH_3 as	1475	60	δCH_3 as	1478 1474	44 48	νC=C ring δCH_3 as			
1430							1442	29	δCH_3 s			
1392	1427	96	δCH_3 s	1425	31	δCH_3 s						
1291	1307	40	wCH_2									
1277				1270	242	$\nu C_{(ring)}$-O				1277	26	wCH_2
1268	1261	638	$\nu C_{(ring)}$-O				1254	206	$\nu C_{(ring)}$-O			
1207				1217	393	ρCH_3						
1198	1200	248	ρCH_3									
1181	1171	117	ρCH_3	1176	60	ρCH_3						
1152	1156	70	δCH ring									
1108							1112	60	$\nu C_{(ring)}$-N			
1102				1106	78	$\nu C_{(=O)}$-N						
1080				1080	84	δ ring						
1034				1037	41	$\nu O\text{-}C(H_3)$	1040	56	$\nu O\text{-}C(H_3)$			
1027	1031	274	$\nu O\text{-}C(H_3)$									
994	989	10	δ ring									
985				977	30	ρCH_2						
932										935	17	νCC
880	917	135	$\nu N\text{-}C_{(H2Cl)}$				894	75	skeletal			
832							844	34	γCH			
808	824	61	νC(=O)N									
799				799	19	γCH						
747	773 752	104 51	δCNC γC=O	743	70	γC=O	767	39	γCH			
721							715	11	δ ring	714	37	νC-Cl
699				683	43	νC-Cl	680	23	τ ring			
684	669	59	νC-Cl	675	49	νC-Cl						

[a] Wavenumbers (ν) in cm^{-1}; calculated infrared intensities (I^{IR}) in km mol^{-1}; ν, stretching; δ, bending; ρ, rocking; g, out-of-plane deformation, τ, torsion, w, wagging; calculated frequencies were scaled by 0.980 below 2000 cm^{-1} and by 0.960 above. Calculated frequencies without experimental counterparts are omitted.

In the 2300–2100 cm^{-1} region of the spectra of the photolyzed matrices (Figure 7), prominent bands are observed at 2263 cm^{-1} and in the 2183–2128 cm^{-1} range. These bands fit well the predicted vibrational data for isocyanate **2** and carbodiimide **4**, respectively, and their positions are consistent with the characteristic matrix-isolated bands reported for these species when photogenerated from compounds structurally related to **1** [26,27,42,43]. Additional features of these photoproducts are observed in the fingerprint spectral region (see Figure 8). Indeed, most of the higher intensity bands predicted for these two species are experimentally observed (Table 4). The only intense bands not observed experimentally correspond to those predicted to occur at frequencies overlapping with the reactant species (e.g., the predicted intense band of carbodiimide **4** at 1055 cm^{-1}, see Figure 8).

The observation of the isocyanate can be rationalized by initial formation of an acylnitrene intermediate that promptly undergoes a Curtius-type rearrangement to the corresponding isocyanate [44,45]. Concomitantly with the isocyanate formation, photogeneration of 2-chloroacetonitrile **3** is also expected. This compound is predicted

to originate a low intensity IR spectrum (see Table S2), but its most intense bands, predicted at 1277, 935 and 714 cm^{-1} by the calculations can be tentatively assigned to experimental counterparts at 1277, 932 and 721 cm^{-1}. The second band, in particular, even though being of very low intensity, appears to be a good mark band of this compound in the photolyzed matrix spectra, since it is ascribed only to this photoproduct, while the other two are also assigned to another photoproduced species (the cyanamide **5** and isocyanate **2**, see Table 4).

The carbodiimide **4** is a product of rearrangement of **1** upon ring opening via N−O bond cleavage and most likely proceeds through an imidoylnitrene intermediate, which rapidly rearranges to the carbodiimide following a Curtius-type mechanism. The carbodiimide is, according to the estimations for reaction branching, based on the relative intensities of the bands of the isocyanate **2** and carbodiimide **4** in the observed spectra, the favored photoproduct of **1**. According to our estimations, these two species exist in the spectrum recorded after 60 min of irradiation (λ = 255 nm) in an approximately 2:1.5 population ratio.

Two other photoproducts could also be identified: CO, as testified by observation of its characteristic band at 2139 cm^{-1} [46,47], and that is a result of unidentified secondary reactions, and cyanamide **5**, which probably results from a rearrangement of the carbodiimide **4** and has band marks observed at 2234, 1728, 1595, 1207, 1102, 1080, 985 and 799 cm^{-1}, besides the band at 1277 cm^{-1} ($\nu C_{(ring)}$–O) already mentioned above. The experimental cyanamide bands have correspondence in the intense calculated bands for this compound at 2244 (νNCN as), 1735 (νC=O), 1604 (νC=C ring), 1217 (ρCH_3), 1106 ($\nu C_{(C=O)}$–N), 1080 (δ ring), 977 (ρCH_2) and 799 (γCH) cm^{-1} (see Table 4). According to the estimations of the relative amounts of the identified photoproducts in the photolyzed matrix, the cyanamide **5** amount is ca. half of that of the carbodiimide **4**. If the cyanamide results from a rearrangement of the carbodiimide, than the branch ratio for the reactions leading to these two compounds vs. that leading to formation of the isocyanate (plus 2-chloroacetonitrile) is about 2:1. It shall also be pointed out that the global efficiency of the reactions undergone by **1** is relatively low, since after 60 min. only about 15 % of the reactant was found to react.

One has also considered the possibility of formation of other species, like the diazirine **6**, nitrilimine **7** and 1,3,4-oxadiazole **8** (see Scheme 2), but data do not support the presence of these species in the photolyzed matrix. For example, the vibrational calculations predict a strong absorption band for nitrilimine **7** at 1339 cm^{-1}, which has no corresponding feature in the experimental spectrum recorded after irradiation. In the case of the diazirine **6** and 1,3,4-oxadiazole **8**, calculations predict intense mark bands at 1110 and 1545 cm^{-1}, respectively, which have no experimental counterpart too.

The absence of the nitrile imine **7** and diazirine **6** is consistent with numerous literature reports demonstrating that nitrile imines are highly reactive intermediates. These species typically rearrange to diazirines and imidoylnitrenes and then to carbodiimides [26,42,43,48–51]. In fact, this photorearrangement sequence is unidirectional; under photochemical conditions, nitrile imines and diazirines readily convert to carbodiimides via low activation barriers, typically estimated at < 26 kJ mol^{-1} for the final 1,2-shift in related systems [48], whereas the reverse process is not observed. Therefore, under our experimental conditions, the efficient formation of carbodiimide **4** from **1** with the intermediacy of imidoylnitrene precludes the generation of diazirine **6** or nitrile imine **7**, and of substituted 1,3,4-oxadiazole **8**. While these results are primarily governed by the kinetic barriers of the rearrangement manifold, the observed experimental outcomes are also aligned with the computed relative energies of all putative photoproducts (Table S1). Although these values provide a thermodynamic guideline rather than a full kinetic description, the species observed experimentally correspond to the energetically most favorable species. The isocyanate **2** (plus 2-chloroacetonitrile), carbodiimide **4** and the cyanamide **5** are more stable than the reactant species **1** by ca. −58, −54 and −48 kJ mol^{-1}. On the other hand, the non-observed putative photoproducts **6**, **7** and **8**, have relative energies amounting to ca. 172, 105 and −24 kJ mol^{-1} relative to the reactant (see Table S1), with the first two being particularly unfavorable.

4. Conclusions

In this work, we have provided the first comprehensive characterization of the conformational preferences, vibrational properties, and intrinsic photochemistry of 3-chloromethyl-5-(3-methoxyphenyl)-1,2,4-oxadiazole (CMPO) under isolated-molecule conditions. Quantum-chemical calculations showed that the molecule may adopt eight conformers, of which only the four *skew* forms (where the C–Cl bond is tilted out of the oxadiazole ring plane) contribute significantly to the equilibrium gas-phase conformational ensemble. The sizeable energy barriers associated with methoxy and inter-ring rotations ensure conformational trapping at cryogenic temperatures, enabling all four *skew* conformers to be stabilized in solid N_2 at 15 K. Comparison of the experimental infrared spectrum with B3LYP/6-311++G(d,p) calculations confirmed the simultaneous presence of these four conformers in the as-deposited matrix.

The UV absorption spectra of CMPO in solution were found to be well described by TD-DFT calculations and dominated by a strong $S_0 \rightarrow S_2$ ($\pi \rightarrow \pi^*$) transition near 255 nm. Guided by these results, UV irradiation experiments (λ = 255 nm, as well as broadband λ > 220 nm) were performed on the matrix-isolated molecule. The photochemistry of CMPO was shown to proceed primarily through cleavage of the N–O bond of the heterocycle, triggering ring opening and rearrangement. Two major reaction channels were identified: (i) formation of carbodiimide, which was demonstrated to be the preferred photoproduct, and (ii) Curtius-type rearrangement of an acylnitrene intermediate yielding an isocyanate together with 2-chloroacetonitrile. Further secondary rearrangement of the carbodiimide produced cyanamide. No experimental evidence was obtained for the presence of diazirine or nitrilimine, consistent with the established understanding that nitrile imines and diazirines are highly reactive, transient species that undergo unidirectional rearrangement toward carbodiimides. Under the experimental conditions, the overall photochemical efficiency remained modest, with approximately 15% of the trapped molecules reacting after 60 min irradiation; nonetheless, the spectroscopic signatures of all identified photoproducts were found to be in excellent agreement with the computed vibrational data.

Altogether, these results demonstrate that CMPO follows photochemical pathways analogous to those previously reported for other oxadiazole systems, while providing the first solvent-free mechanistic picture for a 3-chloromethyl-substituted 1,2,4-oxadiazole. The present study also highlights the combined value of matrix-isolation infrared spectroscopy and quantum-chemical modelling in elucidating reactive intermediates and photorearrangement routes of complex heteroaromatic systems.

Supplementary Materials

The additional data and information can be downloaded at: https://media.sciltp.com/articles/others/26070110 29385985/PS-25120188-SM.pdf. Figure S1: with the comparison between the photochemistry results obtained with narrowband UV irradiation (λ = 255 nm) and broadband (λ > 220 nm) irradiation of matrix-isolated CMPO (**1**); Table S1: with the calculated zero-point corrected energies for the conformers of CMPO and putative photoproducts; Table S2: with calculated vibrational frequencies and infrared intensities for the most relevant conformers of CMPO and for the most stable conformers of the observed photoproproducts isocyanate (**2**) and 2-chloroacetonitrile (**3**); Table S3: with calculated vibrational frequencies and infrared intensities for the most stable conformers of observed and non-observed photoproducts carbodiimide (**4**), cyanamide (**5**), diazirine (**6**), nitrilimine (**7**) and 1,3,4-oxadiazole (**8**); Computational Data: Cartesian coordinates for the B3LYP/6-311++G(d,p) optimized geometries of the species described in this article.

Author Contributions

İ.S.: Investigation, computations, writing—original draft; A.J.L.J.: Writing—review and editing, computations, visualization, conceptualization; R.F.: writing—review and editing, resources, supervision, project administration. All authors have read and agreed to the published version of the manuscript.

Funding

The authors acknowledge the financial support from the Portuguese "*Fundação para a Ciência e a Tecnologia*" (FCT), through Projects CQC-IMS UIDB/00313/2025 and UIDP/00313/2025 (national funds; DOI: 10.54499/UIDB/00313/2025 and 10.54499/UIDP/00313/2025) and LA/P/0056/2025. İ.S. also acknowledges Bitlis Eren University Research Foundation through project BEBAP-2022.23 and the Scientific and Technological Research Council of Türkiye (TÜBİTAK) for a grant offered under the 2219-Postdoctoral Research Fellowship Program. The Horizon-Widera-2023-Talents-01 ERA-Chair 1011848998 Spectroscopy@IKU "*Manipulating and Characterizing Molecular Architectures: From Isolated Molecules to Molecular Crystals*" is Funded by the European Union.

Institutional Review Board Statement

Not applicable.

Informed Consent Statement

Not applicable.

Data Availability Statement

The data supporting this article has been included as part of the Supplementary Information.

Conflict of Interest Disclosure

The authors declare no conflict of interest.

Use of AI and AI-Assisted Technologies

No AI tools were utilized for this paper.

References

1. Pace, A.; Pierro, P. The new era of 1,2,4-oxadiazoles. *Org. Biomol. Chem.* **2009**, *7*, 4337–4348.
2. Cherkasova, A.; Astolfi, R.; Nawrozkij, M.; et al. 1,2,4-Oxadiazoles in medicinal chemistry: Trends of the last years. *Eur. J. Med. Chem.* **2025**, *297*, 117935.
3. Pace, A.; Buscemi, S.; Piccionello, A.P.; et al. Recent Advances in the Chemistry of 1,2,4-Oxadiazoles. *Adv. Heterocycl. Chem.* **2015**, *116*, 85–136.
4. Camci, M.; Karali, N. Bioisosterism: 1,2,4-Oxadiazole Rings. *ChemMedChem* **2023**, *18*, e202200638.
5. Khasawneh, H.E.N.; Alrikabi, A.A.A.; Al-Erjan, A.M.; et al. Unveiling the therapeutic potential of 1,2,4-oxadiazole derivatives: An updated review. *Results Chem.* **2025**, *15*, 102271.
6. Biernacki, K.; Daśko, M.; Ciupak, O.; et al. Novel 1,2,4-Oxadiazole Derivatives in Drug Discovery. *Pharmaceuticals* **2020**, *13*, 111.
7. Zhang, H.-Z.; Zhao, Z.-L.; Zhou, C.-H. Recent advance in oxazole-based medicinal chemistry. *Eur. J. Med. Chem.* **2018**, *144*, 444–492.
8. Hendawy, O.M. A comprehensive review of recent advances in the biological activities of 1,2,4-oxadiazoles. *Arch. Pharm.* **2022**, *355*, 2200045.
9. Zhong, L.; Wu, C.; Li, M.; et al. 1,2,4-Oxadiazole as a potential scaffold in agrochemistry: A review. *Org. Biomol. Chem.* **2023**, *21*, 7511–7524.
10. Li, Q.; Cui, L.-S.; Zhong, C.; et al. Asymmetric Design of Bipolar Host Materials with Novel 1,2,4-Oxadiazole Unit in Blue Phosphorescent Device. *Org. Lett.* **2014**, *16*, 1622–1625.
11. Salassa, G.; Terenzi, A. Metal Complexes of Oxadiazole Ligands: An Overview. *Int. J. Mol. Sci.* **2019**, *20*, 3483.
12. Raccuglia, R.; Pibiri, I.; Buscemi, S.; et al. On the Photoreaction of Some 1,2,4-Oxadiazoles in the Presence of 2,3-Dimethyl-2-butene. Synthesis of N-Imidoylaziridines. *Heterocycles* **2007**, *71*, 1529–1537.
13. Newman, H. Photochemistry of 3,5-diphenyl-1,2,4-oxadiazole I. Photolysis in aprotic media. *Tetrahedron Lett.* **1968**, *9*, 2417–2420.
14. Buscemi, S.; Pace, A.; Pibiri, I.; et al. Competing Ring-Photoisomerization Pathways in the 1,2,4-Oxadiazole Series. An Unprecedented Ring-Degenerate Photoisomerization. *J. Org. Chem.* **2002**, *67*, 6253–6255.
15. Vivona, N.; Buscemi, S.; Asta, S.; et al. Photoinduced molecular rearrangements. The photochemistry of 1,2,4-oxadiazoles in the presence of sulphur nucleophiles. Synthesis of 1,2,4-thiadiazoles. *Tetrahedron* **1997**, *53*, 12629–12636.
16. Vivona, N.; Buscemi, S. Photoinduced molecular rearrangements of ON bond-containing five-membered heterocycles. An assay for 1,2,4- and 1,2,5-oxadiazoles. *Heterocycles* **1995**, *41*, 2095–2116.
17. Pace, A.; Pibiri, I.; Buscemi, S.; et al. Molecular Rearrangements of 1-Oxa-2-azoles as an Expedient Route to Fluorinated Heterocyclic Compounds. *Heterocycles* **2004**, *63*, 2627–2648.
18. Buscemi, S.; Pace, A.; Vivona, N.; et al. Photoinduced Single Electron Transfer on 5-Aryl-1,2,4-oxadiazoles: Some Mechanistic Investigations in the Synthesis of Quinazolin-4-ones. *J. Org. Chem.* **1999**, *64*, 7028–7033.
19. Buscemi, S.; Cicero, M.G.; Vivona, N.; et al. Photochemical behaviour of some 1,2,4-oxadiazole derivatives. *J. Chem. Soc. Perkin Trans. 1* **1988**, 1313–1315. https://doi.org/10.1039/P19880001313
20. Buscemi, S.; Pace, A.; Vivona, N.; et al. Photoinduced molecular rearrangements. Some comments on the ring-photoisomerization of 1,2,4-oxadiazoles into 1,3,4-oxadiazoles. *J. Heterocycl. Chem.* **2001**, *38*, 777–780.
21. Buscemi, S.; D'Auria, M.; Pace, A.; et al. Theoretical study of photoinduced ring-isomerization in the 1,2,4-oxadiazole series. *Tetrahedron* **2004**, *60*, 3243–3249.
22. Su, M.-D. Model Study of the Photochemical Rearrangement Pathways of 1,2,4-Oxadiazole. *ChemPhysChem* **2014**, *15*, 2712–2722.
23. Pace, A.; Buscemi, S.; Vivona, N.; et al. Photochemistry of 1,2,4-Oxadiazoles. A DFT Study on Photoinduced Competitive Rearrangements of 3-Amino- and 3-N-Methylamino-5-perfluoroalkyl-1,2,4-oxadiazoles. *J. Org. Chem.* **2006**, *71*, 2740–2749.
24. Piccionello, A.P.; Pace, A.; Buscemi, S. Rearrangements of 1,2,4-Oxadiazole: "One Ring to Rule Them All". *Chem. Heterocycl. Compd.* **2017**, *53*, 936–947.
25. Vörös, T.; Lajgút, G.G.; Magyarfalvi, G.; et al. Photochemical Formation of Diazenecarbaldehyde (HNNCHO) and Diazenecarbothialdehyde (HNNCHS) in Low-Temperature Matrices. *J. Phys. Chem. A* **2018**, *122*, 1034–1044.

26. Sıdır, İ.; Lopes, S.; Paixão, J.A.; et al. Structure, IR spectrum and UV-induced photochemistry of a pyridyl-substituted 1,3,4-oxadiazole-thione in Ar matrix and intermolecular interactions in the neat crystalline phase. *J. Photochem. Photobiol. A* **2026**, *470*, 116610.
27. Sıdır, İ.; Lopes, S.; Fausto, R.; et al. Molecular Structure, Matrix-Isolation IR Spectrum and UV-Induced Transformations of 2-Amino-5-(4-Methoxyphenyl)-1,3,4-Oxadiazole. *Molecules* **2025**, *30*, 3444.
28. Frisch, M.J.; Trucks, G.W.; Schlegel, H.B.; et al. *Gaussian 16*, Revision B.01; Gaussian, Inc.: Wallingford, CT, USA, 2016.
29. Becke, A.D. A new mixing of Hartree–Fock and local density-functional theories. *J. Chem. Phys.* **1993**, *98*, 1372–1377.
30. Lee, C.; Yang, W.; Parr, R.G. Development of the Colle-Salvetti correlation-energy formula into a functional of the electron density. *Phys. Rev. B* **1988**, *37*, 785–789.
31. Vosko, S.H.; Wilk, L.; Nusair, M. Accurate spin-dependent electron liquid correlation energies for local spin density calculations: A critical analysis. *Can. J. Phys.* **1980**, *58*, 1200–1211.
32. Krishnan, R.; Binkley, J.S.; Seeger, R.; et al. Self-consistent molecular orbital methods. XX. A basis set for correlated wave functions. *J. Chem. Phys.* **1980**, *72*, 650–654.
33. Clark, T.; Chandrasekhar, J.; Spitznagel, G.W.; et al. Efficient diffuse function-augmented basis sets for anion calculations. III. The 3–21+G basis set for first-row elements, Li–F. *J. Comput. Chem.* **1983**, *4*, 294–301.
34. Zhurko, G.A. Chemcraft—Graphical Software for Visualization of Quantum Chemistry Computations. Version 1.8. Available online: www.chemcraftprog.com (accessed on 15 November 2025).
35. Dennington, R.; Keith, T.A.; Millam, J.M. *GaussView*, Version 6; Semichem Inc.: Shawnee Mission, KS, USA, 2016.
36. Runge, E.; Gross, E.K.U. Density-Functional Theory for Time-Dependent Systems. *Phys. Rev. Lett.* **1984**, *52*, 997–1000.
37. Barnes, A.J. Matrix isolation vibrational spectroscopy as a tool for studying conformational isomerism. *J. Mol. Struct.* **1984**, *113*, 161–174.
38. Lopes Jesus, A.J.; Rosado, M.T.S.; Reva, I.; et al. Conformational Study of Monomeric 2,3-Butanediols by Matrix-Isolation Infrared Spectroscopy and DFT Calculations. *J. Phys. Chem. A* **2006**, *110*, 4169–4179.
39. Reva, I.; Lopes Jesus, A.J.; Rosado, M.T.S.; et al. Stepwise conformational cooling towards a single isomeric state in the four internal rotors system 1, 2-butanediol. *Phys. Chem. Chem. Phys.* **2006**, *8*, 5339–5349.
40. Lopes Jesus, A.J.; Rosado, M.T.S.; Reva, I.; et al. Structure of Isolated 1,4-Butanediol: Combination of MP2 Calculations, NBO Analysis, and Matrix-Isolation Infrared Spectroscopy. *J. Phys. Chem. A* **2008**, *112*, 4669–4678.
41. Rosado, M.T.S.; Lopes Jesus, A.J.; Reva, I.; et al. Conformational Cooling Dynamics in Matrix-Isolated 1,3-Butanediol. *J. Phys. Chem. A* **2009**, *113*, 7499–7507.
42. Bégué, D.; Qiao, G.G.; Wentrup, C. Nitrile Imines: Matrix Isolation, IR Spectra, Structures, and Rearrangement to Carbodiimides. *J. Am. Chem. Soc.* **2012**, *134*, 5339–5350.
43. Ferreira, G.A.; Nunes, C.M.; Lopes Jesus, A.J.; et al. The *meta* and *para* OH Substitution Effect on *C*-Phenyl-Nitrilimine Bond-Shift Isomers. *Eur. J. Org. Chem.* **2023**, *26*, e202300310.
44. Curtius, T. Ueber Stickstoffwasserstoffsäure (Azoimid) N_3H. *Ber. Dtsch. Chem. Ges.* **1890**, *23*, 3023–3033.
45. Curtius, T. 20. Hydrazide und Azide organischer Säuren I. Abhandlung. *J. Prakt. Chem.* **1894**, *50*, 275–294.
46. Maki, A.G. Infrared Spectra of Carbon Monoxide as a Solid and in Solid Matrices. *J. Chem. Phys.* **1961**, *35*, 931–935.
47. Lundell, J.; Krajewska, M.; Räsänen, M. Matrix isolation infrared and ab initio study of the 1:1 complex between ammonia and carbon monoxide. *J. Mol. Struct.* **1998**, *448*, 221–230.
48. Fischer, S.; Wentrup, C. Nitrile imide–imidoylnitrene–carbodi-imide rearrangement. *J. Chem. Soc. Chem. Commun.* **1980**, 502–503. https://doi.org/10.1039/C39800000502
49. Nunes, C.M.; Reva, I.; Rosado, M.T.S.; et al. The Quest for Carbenic Nitrile Imines: Experimental and Computational Characterization of C-Amino Nitrile Imine. *Eur. J. Org. Chem.* **2015**, *2015*, 7484–7493.
50. Bégué, D.; Santos-Silva, H.; Dargelos, A.; et al. Imidoylnitrenes R′C(═NR)–N, Nitrile Imines, 1H-Diazirines, and Carbodiimides: Interconversions and Rearrangements, Structures, and Energies at DFT and CASPT2 Levels of Theory. *J. Phys. Chem. A* **2017**, *121*, 8227–8235.
51. Lopes Jesus, A.J.; Nunes, C.M.; Ferreira, G.A.; et al. Photochemical Generation and Characterization of C-Aminophenyl-Nitrilimines: Insights on Their Bond-Shift Isomers by Matrix-Isolation IR Spectroscopy and Density Functional Theory Calculations. *Molecules* **2024**, *29*, 3497.